Valence tautomerism and spin crossover in pyridinophane-cobalt-dioxolene complexes: an experimental and computational study†

Tina Tezgerevska,[a] Elodie Rousset,[a] Robert W. Gable,[a] Guy N. L. Jameson,[a] E. Carolina Sañudo,[b] Alyona Starikova[c] and Colette Boskovic*[a]

Cite this: Tezgerevska, T.; Rousset, E.; Gable, R. W.; Jameson, G. N. L.; Sañudo, E. C.; Starikova, A.; Boskovic, C. *Dalt. Trans.* **2019**, *48*, 11674–11689.

DOI: 10.1039/c9dt02372k

Abstract

Compounds [Co(L-N_4R_2)(dbdiox)](BPh_4) (L-N_4R_2 = N,N'-di-alkyl-2,11-diaza[3.3]-(2,6)pyridinophane, R = ^{i}Pr (**1a**), Et (**2a**); dbdiox = 3,5-di-*tert*-butyldioxolene) and [M(L-N^{i}Pr$_2$)(dbdiox)](BPh_4) (M = Mn (**3a**), Fe (**4a**)) have been synthesized and investigated with a view to possible valence tautomeric (VT) or spin crossover (SCO) interconversions. Single crystal X-ray diffraction data for all compounds at 100 or 130 K indicate trivalent metal cations and di-*tert*-butylcatecholate ($dbcat^{2-}$) dioxolene ligands. Variable temperature magnetic susceptibility data for all species between 2 and 340 K are consistent with these redox states, and low spin configurations for the cobalt(III) ions and high spin for the manganese(III) and iron(III) irons.

Above 340 K, compound **1a** exhibits an increase in magnetic susceptibility, suggesting the onset of a VT interconversion from low spin Co(III)-dbcat to high spin Co(II)-dbsq (dbsq^{-} = di-*tert*-butylsemiquinonate) that is incomplete up to 400 K. In solution, variable temperature electronic absorption spectra, and Evans NMR method magnetic susceptibility data, indicate reversible VT interconversions for **1a** in several solvents, with the transition temperature varying with solvent. Variable temperature electronic absorption spectra are temperature-invariant for **3a** and **4a**, while spectra for **2a** in 1,2-dichloroethane suggest the onset of a VT transition at the highest temperatures measured. Density functional theory calculations on all four compounds and literature analogues provide key insights into the relative energies of the different electromeric forms and the possibilities for VT versus SCO interconversions in this family of compounds.

Introduction

Elucidation of the electronic lability in metal complexes that undergo spin crossover (SCO) or valence tautomeric (VT) transitions remains a fascinating challenge for inorganic chemists. These compounds can be reversibly interconverted between forms with different chemical and physical properties upon application of a stimulus, such as heat, which makes them of interest for future applications in displays, sensors, photoresponsive devices or molecular electronics/spintronics.[1–3] The switching in SCO complexes is due to a spin state transition at a single metal center from low spin (LS) to high spin (HS), which is well-established for complexes of Fe(II), Fe(III), Co(II) and Mn(III).[1,4,5] Very important for SCO is the ligand donor set around the metal center, as the ligand field splitting governs the thermodynamics of the transition. Typical ligand donor sets are specific to the switching metal center, with N-, O- and S-donor ligands the most common. More

complicated are VT transitions, which involve intramolecular electron transfer between a metal and a ligand, often combined with a spin state transition at the metal center. The main exemplar molecules for VT transitions are octahedral cobalt complexes with 3,5-di-*tert*-butyldioxolene (dbdiox) ligands, for which electron transfer from a di-*tert*-butylcatecholate ($dbcat^{2-}$) ligand to the LS-Co(III) ion is coupled with a spin transition, yielding a HS-Co(II) ion bound to a di-*tert*-butylsemiquinonate ($dbsq^{-}$) ligand.[6-8] In these complexes, the LS-Co(III)-dbcat tautomer predominates at low temperature, interconverting to the HS-Co(II)-dbsq form at higher temperature. Cobalt-dioxolene VT complexes typically incorporate N-donor ancillary ligands. The thermal induction of both SCO and VT transitions is largely entropically driven, with the entropy gain arising from the higher density of vibrational states of the high temperature species due to the longer metal-ligand bonds and the higher spin state degeneracy. Like SCO transitions of Fe(II) complexes,[9] VT transitions in cobalt-dioxolene systems can sometimes also be induced by irradiation with visible light.[10]

Twelve-membered tetraazamacrocylic N,N'-dialkyl-2,11-diaza[3.3]-(2,6)pyridinophane (L-N_4R_2; Chart 1) ligands fold upon coordinating to an octahedral metal-center, leaving two *cis* sites vacant for other ligands.[11] In the case of cobalt complexes of such tetradentate N-donor ligands, coordination of a suitable dioxolene ligand in these *cis*-disposed sites might be considered likely to generate a VT transition. However, intriguingly, instead a thermally-induced SCO transition was reported for [Co(L-N_4tBu$_2$)(dbsq)](B(*p*-$C_6H_4Cl)_4$, which remains the only example of a cobalt-dioxolene compound to exhibit SCO, rather than a VT transition.[12,13] Ferromagnetic coupling is evident between the LS-Co(II) ion and the semiquinonate ligand at low temperature, while the nature of the coupling with the HS-Co(II) ion at high temperature is difficult to ascertain. In contrast, use of the pyridinophane azamacrocycle with methyl substitution at the amine position

affords the complex $[Co(L\text{-}N_4Me_2)(dbcat)]^+$; the BPh_4^- salt of this complex contains a LS-Co(III) ion and does not exhibit either SCO or a VT transition.[12,13] The difference between the electronic lability of the complexes with methyl- and *tert*-butyl-substituted macrocyclic ligands is attributed to the steric interaction of the axial *tert*-butyl substituents with the equatorial ligands, which lengthens the bond between the cobalt and the amine nitrogen and reduces the σ-donor capacity of these axial ligands.

Chart 1 Tetradentate pyridinophane ligands and numbering scheme for metal complexes

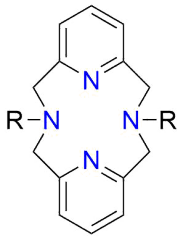

R = Me	$L\text{-}N_4Me_2$	$[Co(L\text{-}N_4Me_2)(dbdiox)]^+$	(**5**)
Et	$L\text{-}N_4Et_2$	$[Co(L\text{-}N_4Et_2)(dbdiox)]^+$	(**2**)
^{i}Pr	$L\text{-}N_4i\text{Pr}_2$	$[M(L\text{-}N_4i\text{Pr}_2)(dbdiox)]^+$	M = Co (**1**), Mn (**3**), Fe(**4**)
^{t}Bu	$L\text{-}N_4t\text{Bu}_2$	$[Co(L\text{-}N_4t\text{Bu}_2)(dbdiox)]^+$	(**6**)

Analogous iron complexes with the methyl-substituted macrocycle exist as $[Fe(L\text{-}N_4Me_2)(dbsq)]^{2+}$, with a LS-Fe(III) center antiferromagnetically coupled to the semiquinonate radical, or as $[Fe(L\text{-}N_4Me_2)(dbcat)]^+$ with a HS-Fe(III) center.[14] In the absence of dioxolene co-ligands, SCO transitions have been observed for iron(II) and iron(III) complexes of $L\text{-}N_4Me_2$ and for iron(II) and cobalt(II) complexes of $L\text{-}N_4t\text{Bu}_2$.[15] The only reported non-dioxolene cobalt(II) complex of $L\text{-}N_4Me_2$ exists only in the high spin state.[15] High spin manganese(II) and manganese(III) complexes of $L\text{-}N_4R_2$ (R = Me, *i*Pr and *t*Bu) ligands are known and do not exhibit electronic lability.[16-19] The $L\text{-}N_4R_2$ family of ligands display remarkable conformational flexibility in their metal complexes.[20] Clearly, very subtle electronic and steric factors govern the redox states and charge distributions in these metal complexes.

In previous work, we have found that the related dinuclear cobalt-bis(dioxolene) complex $[\{Co(L\text{-}N_4tBu_2)\}_2(spiro)]^{2+}$ ($spiroH_4$ = 3,3,3',3'-tetra- methyl-1,1'-spirobis(indane)-5,5',6,6'-tetrol) exists as the mixed-valence $[\{LS\text{-}Co^{III}(L\text{-}N_4tBu_2)\}spiro^{cat-sq}\{LS\text{-}Co^{II}(L\text{-}N_4tBu_2)\}]^{2+}$ form below 150 K, which is interestingly mixed-valence in terms of both metal centers and dioxolene redox sites.[21] The dinuclear complex undergoes a thermally-induced interconversion above 150 K, however we were unable to ascertain whether the transition was SCO at the "Co(II)-semiquinonate" half of the molecule or VT at the "Co(III)-catecholate" half. With a view to examining simpler mononuclear systems, and given our ongoing interest in VT complexes,[22-28] we turned our attention to $L\text{-}N_4iPr_2$ and $L\text{-}N_4Et_2$ pyridinophane ligands, intermediate between the more widely studied methyl and *tert*-butyl derivatives. We report herein the results of our investigation of 3,5-di-*tert*-butyldioxolene complexes of cobalt with the *iso*-propyl-substituted tetraazamacrocyclic ligand $[Co(L\text{-}N_4iPr_2)(dbdiox)]^+$ (**1**), as a comparative study with the ethyl-substituted analogue $[Co(L\text{-}N_4Et_2)(dbdiox)]^+$ (**2**) and the isostructural manganese $[Mn(L\text{-}N_4iPr_2)(dbdiox)]^+$ (**3**) and iron $[Fe(L\text{-}N_4iPr_2)(dbdiox)]^+$ (**4**) complexes (Chart 1). We compare our results with previously reported cobalt complexes $[Co(L\text{-}N_4Me_2)(dbdiox)]^+$ (**5**) and $[Co(L\text{-}N_4tBu_2)(dbdiox)]^+$ (**6**).

Experimental Section

Synthesis

All manipulations were performed under a nitrogen atmosphere using standard Schlenk techniques if not indicated otherwise. All reagents were used as received except where solvents were degassed prior to use. Ferrocenium tetraphenylborate, $[FeCp_2](BPh_4)$, was synthesized as previously

reported.[29] The ligands L-N$_4$*i*Pr$_2$ and L-N$_4$Et$_2$ were synthesized by modification of a method described elsewhere.[30,31]

[Co(L-N$_4$*i*Pr$_2$)(dbdiox)](BPh$_4$)·dioxane (1a·dioxane). A solution of $CoCl_2 \cdot 6H_2O$ (0.123 mmol, 29.3 mg) in isopropanol (2 mL) was degassed and left stirring under N_2 until dissolved, followed by the addition of a solution of L-N$_4$*i*Pr$_2$ (0.123 mmol, 40.0 mg) in isopropanol (2 mL). The reaction was stirred until a uniform blue precipitate was evident. A second solution containing 3,5-di-*tert*-butylcatechol, (0.123 mmol, 27.4 mg) and triethylamine (0.247 mmol, 34.4 μL), in 2.00 mL isopropanol was warmed whilst stirring vigorously under N_2 for 10 minutes. The warm solution was added to the cobalt mixture, resulting in an orange-red solution that was left to stir for a further 10 minutes. Solid [FeCp$_2$](BPh$_4$), (0.123 mmol, 62.1 mg) was added all at once to the brown suspension that appeared on cooling. The mixture was then sonicated for 20 minutes and left stirring overnight. The crude product was collected by vacuum filtration under N_2, washed with diethyl ether and then dissolved in minimum dichloromethane. Layering the saturated dichloromethane solution with dioxane afforded red/orange square plates suitable for X-ray diffraction. The bulk sample was isolated by filtration, washed with diethyl ether and air-dried (101 mg, 81%). Anal. Calcd (found) for $C_{62}H_{76}N_4O_4BCo$: C, 73.65 (73.13); H, 7.58 (7.67); N, 5.54 (5.79). HR-MS (ESI-QTOF) m/z $[M]^+$ Calcd for $C_{34}H_{48}N_4O_2Co$ 603.3109; Found 603.3105. Selected IR data (KBr, cm^{-1}): 1608(m), 1580(m), 1533(w), 1478(s), 1463(sh), 1427(s), 1412(s), 1392(s), 1358(m), 1321(w), 1280(w), 1239(s), 1202(s), 1165(w), 1146(w), 1123(w), 1098(w), 1031(w), 983(m), 907(w), 877(w), 844(w), 817(w), 786(m), 736(s), 710(s), 651(w), 612(m), 548(w).

[Co(L-N$_4$Et$_2$)(dbdiox)](BPh$_4$)·2dioxane (2a·2dioxane). The reaction procedure was analogous to that described for **1a**·dioxane, substituting L-N$_4$Et for L-N$_4$*i*Pr$_2$. The crude product

was recrystallized from slow evaporation of a 1:2 acetone:dioxane mixture, resulting in olive green square plates suitable for X-ray diffraction, (110 mg, 84 %). Anal. Calcd (found) for $C_{64}H_{80}N_4O_6BCo$: C, 71.77 (71.84); H, 7.53 (7.70); N, 5.23 (5.34). HR-MS (ESI-QTOF) m/z $[M]^+$ Calcd for $C_{32}H_{44}N_4O_2Co$ 575.2796; Found 575.2800. Selected IR data (KBr, cm^{-1}): 1609(m), 1581(m), 1555(m), 1479(s), 1462(s), 1438(s), 1424(s), 1413(s), 1388(m), 1357(m), 1319(m), 1280(s), 1240(s), 1204(w), 1163(m), 1118(m), 1096(m), 1079(w), 1048(w), 1031(w), 981(m), 939(w), 901(w), 888(w), 870(m), 849(m), 827(w), 810(w), 785(m), 753(m), 737(s), 710(s), 613(m), 550(w).

[Mn(L-N$_4$*i*Pr$_2$)(dbdiox)](BPh$_4$)·1.5dioxane (3a·1.5dioxane). The reaction procedure was analogous to that described for **1a**·dioxane, substituting in $MnCl_2·4H_2O$, (0.123 mmol, 24.4 mg). The crude product was dissolved in dichloromethane and layered with dioxane, yielding golden yellow plates (90 mg, 70 %). Anal. Calcd (found) for $C_{64}H_{80}N_4O_5BMn$: C, 73.13 (72.97); H, 7.67 (7.69); N, 5.33 (5.78). HR-MS (ESI-QTOF) m/z $[M]^+$ Calcd for $C_{34}H_{48}N_4O_2Mn$; 599.3158; Found 599.3148. Selected IR data (KBr, cm^{-1}): 1606(m), 1579(m), 1562(m), 1470(s), 1454(s), 1430(s), 1412(s), 1393(m), 1359(m), 1318(m), 1279(m), 1254(m), 1234(s), 1211(w), 1166(s), 1123(m), 1097(w), 1068(w), 1035(m), 974(s), 926(w), 909(w), 888(w), 873(w), 849(w), 825(m), 790(w), 750(s), 735(s), 708(s), 650(m), 612(m), 581(w), 549(w).

[Fe(L-N$_4$*i*Pr$_2$)(dbdiox)](BPh$_4$)·dioxane (4a·dioxane). The reaction procedure was analogous to that described for **1a**·dioxane, substituting in $FeCl_2·4H_2O$, (0.123 mmol, 24.4 mg). The crude product was dissolved in dichloromethane and layered with dioxane, yielding poorly crystalline purple square plates (95 mg, 76 %). Anal. Calcd (found) for $C_{62}H_{76}N_4O_4BFe$: C, 73.88 (73.65); H, 7.60 (7.58); N, 5.56 (5.87). HR-MS (ESI-QTOF) m/z $[M]^+$ Calcd for $C_{34}H_{48}N_4O_2Fe$ 600.3127; Found 600.3126. Selected IR data (KBr, cm^{-1}): 1605(s), 1581(s), 1470(s), 1429(s),

1395(m), 1359(w), 1281(m), 1239(w), 1206(w), 1165(m), 1123(w), 1091(w), 1060(w), 1033(s), 981(w), 909(w), 886(w), 853(w), 826(w), 789(w), 735(s), 708(s), 675(w), 655(w), 612(m), 536(w).

[Fe(L-N$_4$*i*Pr$_2$)(dbdiox)](BPh$_4$)·2MeOH (4a·2MeOH). The reaction followed the same procedure as describe for **4a**.dioxane. The crude product was dissolved in dichloromethane and layered with methanol, yielding purple plate-shaped crystals. A suitable crystal was handpicked for structural analysis, and although a pure bulk sample was obtained, the product lost crystallinity quickly due to desolvation.

Single Crystal X-ray Data Collection and Structure Solution

Crystals were transferred directly from mother liquor to oil to prevent solvent loss. The crystallographic data (Table 1) for **2a**·2dioxane and **3a**·1.5dioxane, were collected at 130 K using a Rigaku Oxford Diffraction SuperNova Dual Wavelength single crystal X-ray diffractometer using Cu-Kα radiation (λ = 1.5418 Å). Data reduction was performed using CrysAlisPro software (Version 1.171.38.41)[32] using a numerical absorption correction based on Gaussian integration over a multifaceted crystal model. As crystals of **1a**·dioxane and **4a**·2MeOH were small and poorly diffracting data for these two compounds were collected at the MX1 beamline at the Australian Synchrotron,[33] with the wavelength tuned to Mo-Kα radiation (λ = 0.71073 Å). Using the Olex2 software,[34] the structures were solved using the intrinsic phasing routine in SHELXT[32] and refined using a full-matrix least squares procedure based on F^2 using SHELXL.[35,36] All non-hydrogen atoms were refined with anisotropic displacement parameters, while all hydrogen atoms were placed at geometrical estimates and refined using the riding model. For **3a**·1.5dioxane one of the dioxane molecules was disordered over two orientations while for **4a**·2MeOH one of the *tert*-butyl groups

was disordered over two orientations. For both structures the two disordered components were restrained to similar geometry; the final occupancy values were 0.874(3) and 0.126(3), and 0.870(4) & 0.130(4), respectively.**Table 1** Crystallographic data for compounds **1a**·dioxane, **2a**·2dioxane, **3a**·1.5dioxane and **4a**·2MeOH.

	1a·dioxane	**2a**·2dioxane	**3a**·1.5dioxane	**4a**·2MeOH
Empirical formula	$C_{62}H_{76}BCoN_4O_4$	$C_{64}H_{80}BCoN_4O_6$	$C_{64}H_{80}BMnN_4O_5$	$C_{60}H_{76}BFeN_4O_4$
Formula weight	1011	1071.06	1051.07	983.9
Temperature/K	100(2)	130.0(1)	130.0(1)	100(2)
Crystal system	Monoclinic	Triclinic	Triclinic	Monoclinic
Space group	$P2_1/n$	$P\bar{1}$	$P\bar{1}$	$P2_1/n$
a/Å	20.630(4)	11.0684(4)	10.9915(2)	20.520(4)
b/Å	13.870(3)	11.8545(4)	13.6672(4)	13.190(3)
c/Å	21.090(4)	22.1063(8)	19.4001(6)	22.390(5)
α/°	90	95.654(3)	99.531(3)	90
β/°	113.24(3)	92.389(3)	94.045(2)	114.96(3)
γ/°	90	99.975(3)	93.356(2)	90
V/Å^3	5545(2)	2837.72(18)	2859.65(14)	5494(2)
Z	4	2	2	4
ϱ_{calc} g/cm^3	1.211	1.253	1.221	1.189
μ/mm^{-1}	0.36	2.802	2.284	0.323
F(000)	2160	1144	1124	2108
Crystal size/mm^3	0.133×0.112×0.017	0.363×0.126×0.093	0.687×0.287×0.069	0.172×0.122×0.011
Radiation	Synchrotron (λ = 0.71073)	CuKα (λ = 1.54184)	CuKα (λ = 1.54184)	Synchrotron (λ = 0.71073)
2Θ range for data collection/°	2.338 to 63.898	7.616 to 148.14	7.372 to 154.266	2.26 to 63.788
Index ranges	$-27 \le h \le 30$, $-18 \le k \le 20$, $-30 \le l \le 31$	$-9 \le h \le 13$, $-14 \le k \le 12$, $-27 \le l \le 27$	$-9 \le h \le 13$, $-15 \le k \le 17$, $-24 \le l \le 24$	$-29 \le h \le 29$, $-19 \le k \le 19$, $-33 \le l \le 33$
Reflections collected	204924	20930	22065	201292
Independent reflections	17540 [R_{int} = 0.0399, R_{sigma} = 0.0190]	11189 [R_{int} = 0.0261, R_{sigma} = 0.0389]	11754 [R_{int} = 0.0357, R_{sigma} = 0.0451]	16183 [R_{int} = 0.0502, R_{sigma} = 0.0243]
Data/restraints/parameters	17540/0/660	11189/0/693	11754/48/742	16183/12/660
Goodness-of-fit on F^2	1.043	1.045	1.028	1.044
Final R indexes [$I \ge 2\sigma(I)$]	R_1 = 0.0398, wR_2 = 0.0491	R_1 = 0.0386, wR_2 = 0.1014	R_1 = 0.0368, wR_2 = 0.0925	R_1 = 0.0688, wR_2 = 0.2010

Final *R* indexes [all data]	$R_1 = 0.1027$, $wR_2 = 0.1080$	$R_1 = 0.0421$, $= 0.1041$	wR_2	$R_1 = 0.0441$, $= 0.0975$	wR_2	$R_1 = 0.0813$, $= 0.2124$	wR_2
Larg. diff. peak/hole/e Å^{-3}	0.52/-0.59	0.50/-0.31		0.38/-0.38		1.19 / -1.10	

Electrochemistry

Electrochemical measurements were performed in acetonitrile at room temperature using a standard three-electrode configuration connected to an eDAQ computer-controlled potentiostat. Measurements were performed under a continuous nitrogen flow. The three-electrode system for cyclic voltammetry consisted of a 1.0 mm diameter glassy carbon electrode (Cypress Systems), a platinum wire auxiliary electrode and a commercially available Ag/AgCl reference electrode (eDAQ). For rotating disk electrode (RDE) voltammetry a 3 mm glassy carbon (Metrohm) working electrode was employed, connected to a Metrohm rotator. Analyte solutions of 1 mM were prepared in solvent containing 0.25 M Bu_4NPF_6 as the supporting electrolyte. All potentials have been referenced *versus* the ferrocene/ferrocenium redox couple, measured immediately afterwards.

Magnetic Measurements

Magnetic measurements in the solid state were carried out in the Unitat de Mesures Magnètiques (Universitat de Barcelona) on polycrystalline samples (*circa* 20 mg) with a Quantum Design SQUID MPMS-XL magnetometer equipped with a 5 T magnet. Diamagnetic corrections were calculated using Pascal's constants and an experimental correction for the sample holder was applied. Magnetic susceptibility and magnetization data were simultaneously fit using the Simplex algorithm in the program PHI.[37]

Solution magnetic measurements employed the Evans NMR method. NMR samples for susceptibility measurements using the Evans method were prepared by dissolving a weighed

amount of the metal compounds in a measured amount of deuterated dichloroethane or acetonitrile solvent. The concentration of the paramagnetic solute was in the range of 5-10 mg mL^{-1}. The temperature-dependent density changes of the solvent were corrected using equations and data from the International Critical Tables.[38–41] The complex solution was transferred into a coaxial 5 mm NMR tube containing a 1 mm capillary with the deuterated diamagnetic solvent and a small amount of *tert*-butanol as references. The residual ^{1}H NMR resonance of the *tert*-butanol methyl group was used for determining the susceptibility in solution.

Mössbauer Spectroscopy

^{57}Fe Mössbauer spectra were measured on multiple samples of **4a**·dioxane (~20 mg) at various temperatures from 295 K to 6 K. Spectra were measured on a Mössbauer spectrometer (Science Engineering & Education Co., MN) equipped with a closed-cycle refrigerator system from Janis Research Co. and SHI (Sumitomo Heavy Industries Ltd.) and a temperature controller from Lakeshore Cryotronics, Inc. Data were collected in constant acceleration mode in transmission geometry with an applied field of 47 mT parallel to the γ-rays.

Other Measurements

Elemental analyses were performed by the Campbell Microanalytical Laboratory, Chemistry Department, University of Otago, New Zealand. High resolution mass spectra (HR-MS) were performed on an Agilent 6520 Accurate-Mass Q-TOF spectrometer on acetonitrile solutions. Variable temperature ultraviolet-visible (UV-Vis) absorption spectra were recorded on an Agilent Cary 60 UV-Vis spectrophotometer in the range 220-1000 nm. Infrared spectra (KBr disk) were

recorded on a Bruker Tensor 27 FTIR spectrometer. Band intensities are described as strong (s), medium (m), weak (w) or shoulder (sh).

Density Functional Theory Calculations

The DFT calculations were performed using the Gaussian 09 program package[42] with the UTPSSh functional[43,44] and the 6-311++G(d,p) basis set. This methodology reproduces well the energy parameters of spin-state switching rearrangements.[45–47] The stationary points on the potential energy surfaces (PESs) were located by full geometry optimization with calculation of force constants and checked for the stabilities of DFT wave function. Exchange coupling of unpaired electrons in the paramagnetic centers was estimated using the "broken symmetry" (BS) approach.[48] The exchange coupling constants J (in cm^{-1}; $\hat{H} = -2J\mathbf{S}_1\cdot\mathbf{S}_2$) were calculated with the use of Yamaguchi equation.[49] Structural visualizations were prepared using the ChemCraft software[50] with the calculated atomic coordinates as input parameters (Supplementary Information).

Results and Discussion

Syntheses

The synthesis of salts of complexes **1**-**4** was based on the previously reported synthesis of **5** and **6**,[12] involving first binding the pyridinophane ancillary ligand to the divalent metal center, followed by addition of deprotonated 3,5-di-*tert*-butylcatechol. The first stages of the reaction are performed under inert atmosphere to ensure ligand binding prior to oxidation of the metal. The addition of an equivalent of ferrocenium tetraphenylborate to a suspension of the metal complex affords clean oxidation of the metal centers, allowing ready isolation of tetraphenylborate salts of the target complexes in good yield. This was an improvement over the previously reported method

of oxidation with ferrocenium tetrafluoroborate followed by metathesis to exchange the counteranion (for the literature complex **6**, the dioxolene ligand oxidizes in preference to the cobalt).[12] Allowing the complexes to instead oxidize by exposure of the reaction mixture to air affords less tractable crude products. All compounds are soluble in a range of common organic solvents. The purity of the bulk samples is evident from elemental analysis.

Structure Description

The single crystal X-ray diffraction data for compounds **1a**·dioxane, **2a**·2dioxane, **3a**·1.5dioxane and **4a**·2MeOH are available in Table 1. Structural representations of complexes **1** in **1a**·dioxane, **2** in **2a**·2dioxane, **3** in **3a**·1.5dioxane and **4** in **4a**·2MeOH are presented in Fig. 1. Selected interatomic distances and angles are provided in Table 2.

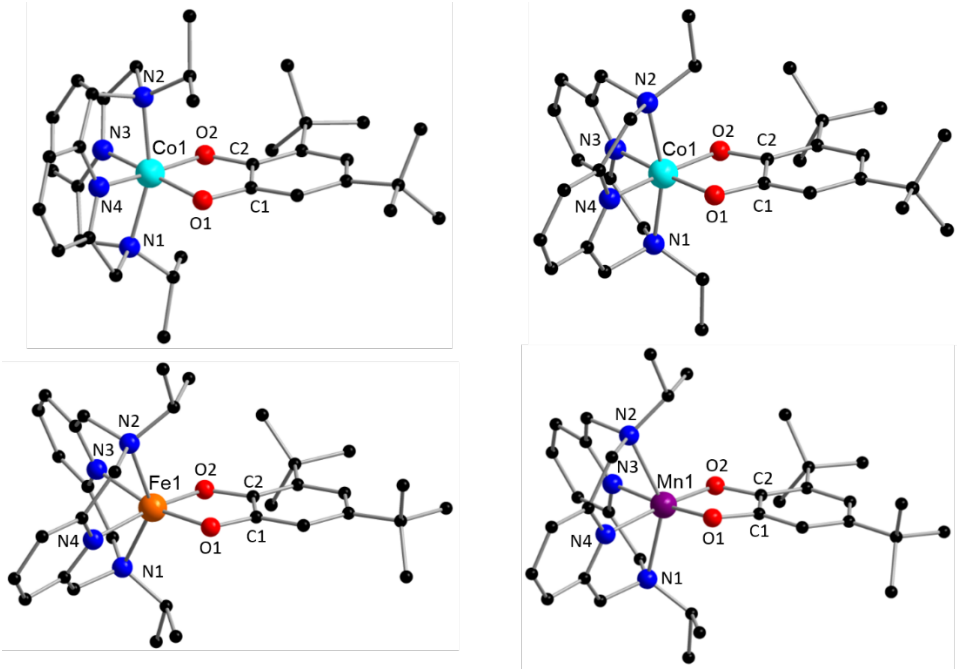

Fig. 1 Molecular structures of (clockwise from top left) **1** in **1a**·dioxane, **2** in **2a**·2dioxane, **3** in **3a**·1.5dioxane and **4** in **4a**·2MeOH. Color code: C (black), N (blue), O (red), Co (aqua), Fe (orange), Mn (violet).

Table 2 Selected Interatomic Distances (Å), Angles (°) and structural parameters for compounds **1a**·dioxane, **2a**·2dioxane, **3a**·1.5dioxane and **4a**·2MeOH.

	1a·dioxane	**2a**·2dioxane	**3a**·1.5dioxane	**4a**·2MeOH
M-O1	1.8784(8)	1.882(1)	1.862(1)	1.943(2)
M-O2	1.8855(8)	1.876(1)	1.862(1)	1.911(2)
M-N1	2.037(1)	2.029(1)	2.325(1)	2.237(2)
M-N2	2.037(1)	2.011(1)	2.313(1)	2.260(2)
M-N3	1.867(1)	1.866(1)	2.014(1)	2.071(2)
M-N4	1.873(1)	1.859(1)	2.035(1)	2.075(2)
C1-O1	1.357(1)	1.348(2)	1.364(2)	1.360(2)
C2-O2	1.353(1)	1.353(2)	1.363(2)	1.354(2)
C1-C2	1.410(1)	1.411(2)	1.410(2)	1.415(3)
O1-M-O2	87.29(4)	88.30(5)	87.164(4)	84.14(6)
N1-M-N2	160.19(4)	162.35(6)	145.70(4)	143.81(7)
N3-M-N4	95.89(4)	94.60(6)	86.94(5)	87.18(7)
M···M[1]	11.277(2)	11.0684(5)	10.0476(6)	10.339(2)
SHAPE[2]	1.378	0.935	3.102	3.974
MOS[3]	-1.93	-1.88	-2.03	-1.94

[1]closest intermolecular distance

[2]SHAPE index for octahedral geometry *OC-6*, calculated in *SHAPE 2.1*.[51]

[3] Metrical Oxidation State, as described in main text.[53]

Compounds **1a**·dioxane and **4a**·2MeOH crystallize in the monoclinic space group $P2_1/n$ while compounds **2a**·2dioxane and **3a**·1.5dioxane crystallize in the triclinic space group $P\bar{1}$. In all cases, the asymmetric unit contains a mononuclear metal complex, two counteranions and solvent molecules. The metal complexes **1**-**4** exhibit the same molecular connectivity and in each case the metal center posseses a distorted coordination geometry that continuous symmetry measurements indicate is closest to octahedral (Table S1).[51] Cobalt complexes **1** and **2** are less distorted from octahedral geometry than the Fe and Mn analogues **3** and **4**.

The macrocyclic ligands bind such that the two sites *trans* to the oxygen atoms of the dioxolene are occupied by the pyridyl nitrogen atoms. Detailed consideration of the metal and dioxolene-based structural parameters (Table 2) provides important insights into the spin and oxidation state of the metal centers as well as the oxidation state of the dioxolene moieties at the data collection temperature. For the cobalt centers in **1** and **2**, the Co-O, Co-N_{amine} and Co-N_{py} bond lengths are in the ranges 1.88-1.89, 2.01-2.04 and 1.86-1.87 Å, respectively. In general, Co-O/N bonds follow the trend: LS-Co(III) < LS-Co(II) < HS-Co(II), with six coordinate pseudo-octahedral low spin cobalt(II) also characterized by a Jahn-Teller distortion. At the temperature of data collection, the Co-O/N distances measured for **1** and **2** are very similar to the literature compound [Co(L-N_4Me_2)(dbcat)](BPh_4)·0.8MeCN·0.2Et_2O (**5a**·0.8MeCN·0.2Et_2O),[12] consistent with LS-Co(III). In contrast, the geometric parameters are markedly different to those measured for the LS-Co(II) complex **6** in [Co(L-N_4tBu_2)(dbdiox)](B(*p*-$C_6H_4Cl)_4$)(**6a**) at 100 K.[12] The Mn-O/N distances in **3a**·1.5dioxane are similar to previously reported manganese(III) complexes of L-N_4R_2 ligands and consistent with HS-Mn(III), with Jahn-Teller elongation along the Mn-N_{amine} (N1-Mn-

N2) direction.[19] Similarly the Fe-O/N distances in **4a**·2MeOH are consistent with HS-Fe(III) and comparable to previously reported HS-Fe(III) complexes of L-N_4R_2 and catecholate ligands.[14,15,52] Empirical bond valence sum calculations indicate trivalent metal centers for all compounds.

For complexes **1**-**4**, the dioxolene C-O (1.36 ± 2 Å) and C1-C2 (1.41 ± 2 Å) distances (Table 2) are all typical of the values generally observed for dioxolene ligands in the catecholate oxidation state. The empirical metrical oxidation state (MOS) of dioxolene ligands, proposed by Brown *et al*. uses a least-squares fitting of C-C and C-O bond lengths to assign an apparent oxidation state: -1 for a semiquinonate ligand and -2 for a catecholate ligand.[53] The MOS parameters calculated for **1**-**4** are in the range -1.88 to -2.03 and indicate that the dioxolene ligands are in the catecholate state at the temperature of data collection. In summary, the structural data for the four complexes in the compounds measured are consistent with the M(III)-dbcat charge distribution at the temperature of data collection (100 or 130 K).

For compounds **1a**·dioxane and **4a**·2MeOH, four metal complexes are present in the unit cell, related by the 2-fold screw axis parallel to the *b* axis, and the inversion center (Fig. S1). The complexes are arranged pseudo head-to-tail fashion, perpendicular to the *b* axis, separated by layers of counteranions Although the dioxane-crystallized cobalt system does not present any particular intermolecular interactions, the methanol molecules in the iron system are involved in a hydrogen bonding network with the dioxolene ligand through the O1 atom. The structures for compounds **2a**·2dioxane and **3a**·1.5dioxane each contain only two metal complexes per unit cell, generated through an inversion center (Fig. S2). The complexes exhibit a ladder-type arrangement perpendicular to the *b* axis. As per the previous dioxane-containing crystal structure, no particular supramolecular interactions are evident in the packing. The shortest intermolecular M···M distances are in the range 10.0-11.3 Å (Table 2) for the four compounds.

Infrared Spectroscopy

Recent detailed spectroscopic studies of cobalt-dioxolene complexes with tetradentate N-donor ancillary ligands have facilitated the assignment of the catecholate-based bands in the mid-infrared, although bands that can be definitively attributed to the semiquinonate state are less clear.[13,54] The infrared spectra for **1a**·dioxane, **2a**·2dioxane, **3a**·1.5dioxane and **4a**·dioxane, measured at room temperature as pressed KBr disks (Fig. S3), are qualitatively similar, as expected for isostructural complexes with the same counteranion. Three bands characteristic of the dioxolene ligands in the catecholate state are clearly evident in the infrared spectra for **1a**, **2a** and **3a** at *ca.* 1240, 1280 and 1360 cm^{-1}, while two further bands at *ca.* 1410 and 1480 cm^{-1} are associated with both catecholate and semiquinonate forms of the dioxolene ligand. While these dioxolene-based bands are evident in the spectrum of **4a**, the intensity of the three catecholate marker bands in the 1200-1440 cm^{-1} range is less than in the other spectra, which is perhaps flagging some partial semiquinonate character for the dioxolene ligand. The region below 1000 cm^{-1} is dominated by bands attributable to the tetraphenylborate counterion, while bands around 1580 and 1610 cm^{-1}, together with other bands in the range of 1000-1500 cm^{-1} are associated with the pyridinophane ligands.[11,14,16] In summary the room temperature infrared spectra are consistent with the presence of catecholate ligands, although some semiquinonate character cannot be ruled out.

Electronic Absorption Spectroscopy

Following confirmation of the presence of complexes **1-4** in acetonitrile solutions of compounds **1a**-**4a** by mass-spectrometry studies, room temperature electronic absorption spectra (Fig. 2) in

the UV-Visible range (280-1000 nm) were measured in acetonitrile, butyronitrile and 1,2-dichloroethane. For compounds **1a**-**3a**, the spectra remained unchanged over a period of at least several hours under ambient conditions, consistent with solution stability and insensitivity to oxygen. In contrast, the spectra for **4a** change rapidly in air, but not under an nitrogen atmosphere, consistent with the catalytic reaction of the coordinated dbcat^{2-} ligand with oxygen reported previously for the L-N$_4$Me$_2$ analogue of this complex.[52] The data are tabulated in Table S2, with band assignments where possible.

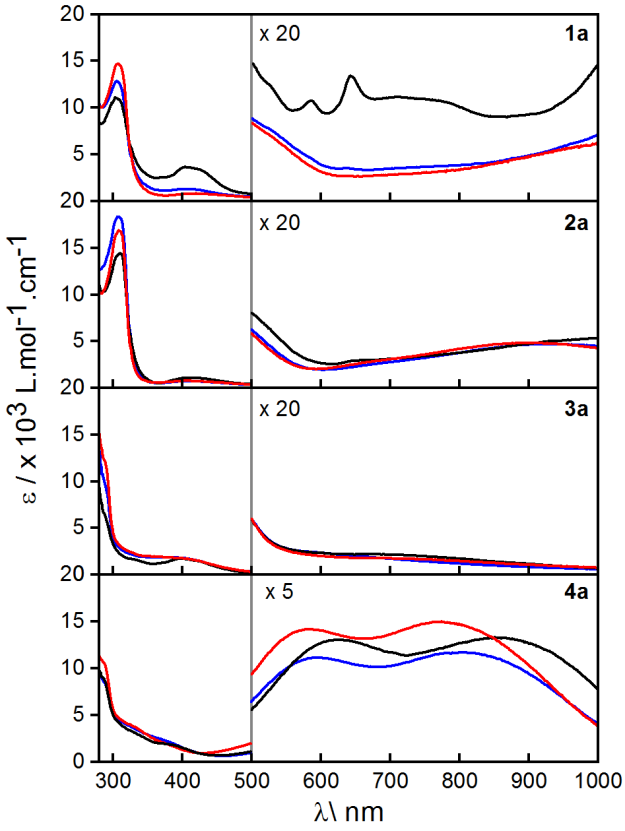

Fig. 2 Electronic absorption spectra (UV-vis) of **1a, 2a, 3a** and **4a** in acetonitrile (red) butyronitrile (blue) and 1,2-dichloroethane (black) at 293 K.

The spectra obtained for cobalt compounds **1a** in acetonitrile and butyronitrile and **2a** in all solvents are characteristic of LS-Co(III)-catecholate chromophores.[24,55] A band between 400 and 420 nm is attributed to a *d-d* transition for six-coordinate Co(III) and a low intensity broad feature between 600 and 1000 nm has been assigned as due to ligand to metal charge transfer (LMCT).[55] The spectrum for **1a** in 1,2-dichloroethane exhibits some additional features, a more intense band around 400 nm, several sharp bands between 500 and 700 nm, a broad feature between 700 and 800 nm as well as the onset of a transition into the near infrared. These features are all suggestive of a HS-Co(II)-semiquinonate chromophore.[11–13,24,55,56] The band at ~ 400 nm is assigned to a Co(II) *d* to *d* transition, the several bands between 500 and 700 nm are assigned as metal to ligand charge transfer (MLCT) transitions and the broad feature between 700 and 800 nm is assigned as internal semiquinonate ligand transitions.[55,56] The onset of a transition in the red going to the near infrared is consistent with a band reported for Co(II)-dbsq complex **6** and assigned as a MLCT band.[13] It appears that at room temperature in 1,2-dichloroethane, complex **1** exists as a mixture of Co(III)-dbcat and Co(II)-dbsq charge distributions.

Variable temperature spectra were also measured for compounds **1a** and **2a** to probe for any VT or SCO interconversions in solution (Figs. 3 and S4). Spectra were measured for **1a** in butyronitrile (278-363 K), 1,2-dichloroethane (283-333 K) and acetonitrile (283-333 K) and **2a** in 1,2-dichloroethane (293-333 K). Distinct and reversible spectral changes are evident for **1a** in butyronitrile and 1,2-dichloroethane, indicating an increased proportion of the Co(II)-dbsq electromer upon heating. An isosbestic or near-isosbestic point is evident between 320 and 340 nm in each case, consistent with the interconversion of two absorbing species. No significant spectral changes are evident in acetonitrile in the measured temperature range. Thus, complex **1** appears to undergo a thermally induced VT interconversion in solution, with the transition

temperature varying with solvent and increasing in the order 1,2-dichloroethane < butyronitrile < acetonitrile. The variable temperature spectra of **2a** in 1,2-dichloroethane, reveal similar reversible changes with an isosbestic point at 325 nm, although the extent of the transition is much less than for **1**, suggesting the onset of a VT transition for complex **2** in this solvent.

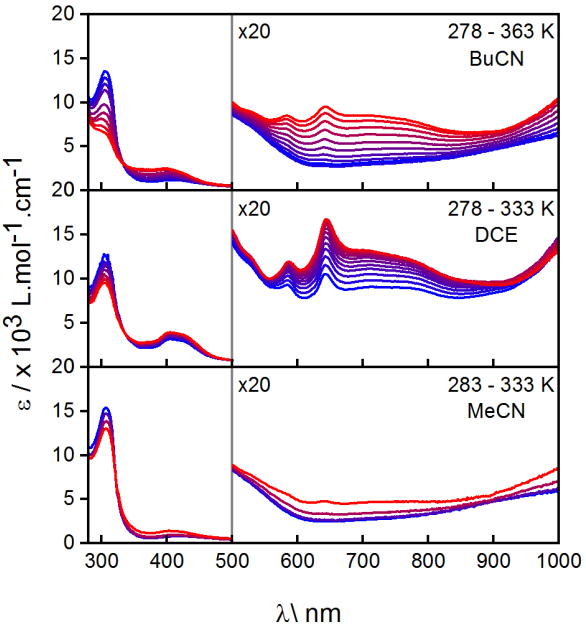

Fig. 3 Variable temperature absorption spectra of **1a** at the indicated temperatures in butyronitrile (BuCN), 1,2-dichloroethane (DCE) and acetonitrile (MeCN).

The room temperature electronic absorption spectra for manganese compound **3a** vary little across the three solvents used (Fig. 2) and are very similar to the spectra of **1a** in acetonitrile and butyronitrile. This is consistent with a Mn(III)-catecholate chromophore.[16,57-61] Variable temperature spectra were also measured for **3a** in butyronitrile (293-333 K) and show little temperature dependence, consistent with no VT or SCO in these temperature ranges (Fig. S4). The room temperature spectra for iron compound **4a** in the different solvents (Fig. 2) are very similar to the

spectrum reported for [Fe^{III}(L-N_4Me_2)(dbcat)],[52] exhibiting a pair of broad bands in the range 500-1000 nm that are more intense than analogous bands for the cobalt and manganese analogues. Similar spectral features are evident for other Fe(III)-catecholate complexes and have been assigned as LMCT transitions.[62] Variable temperature spectra were also measured for **4a** in dichloroethane (293-333 K), but little temperature dependence is evident (Fig. S4), consistent with no VT or SCO in this temperature range.

Electrochemistry

Following confirmation of solution stability via electronic absorption spectroscopy, cyclic and rotating disk electrode (RDE) (Fig. 4) voltammograms were measured for 1 mM solutions of **1a, 2a, 3a** and **4a** in acetonitrile using a glassy carbon electrode. All potentials are referenced to the ferrocene/ferrocenium couple using ferrocene as an internal standard or measured immediately afterwards.

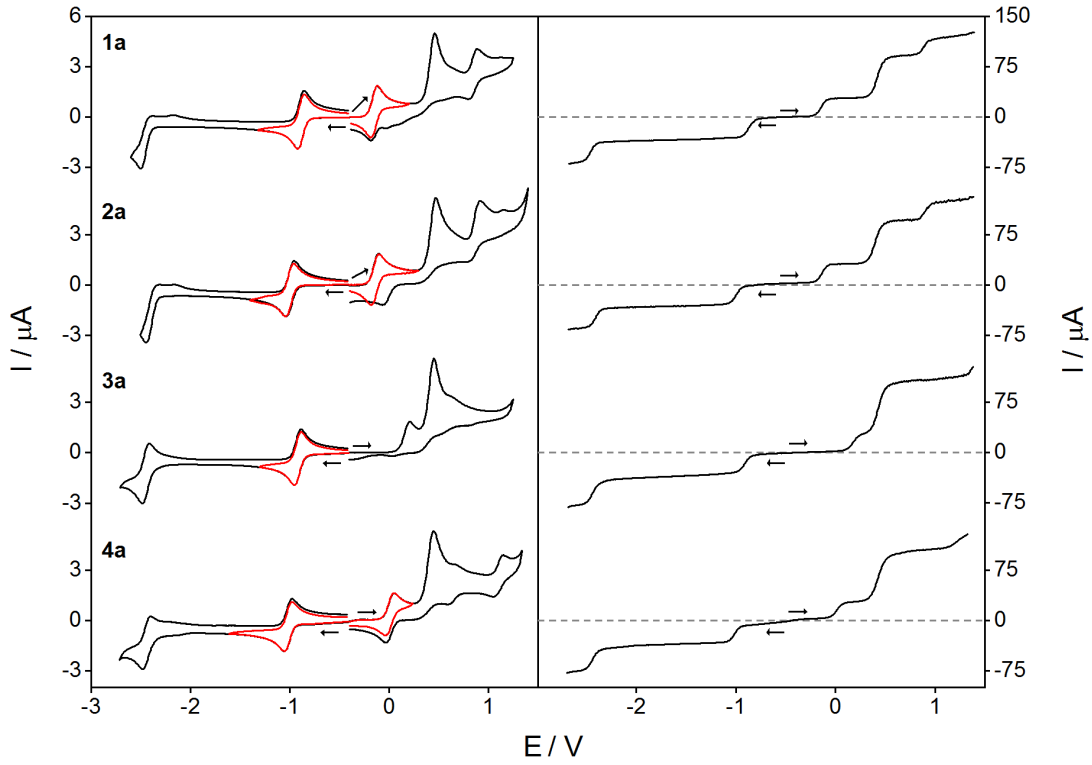

Fig. 4 Cyclic (left) and rotating disk electrode (right) voltammograms of acetonitrile solutions (1.0 mM with 0.25 M Bu_4NPF_6) of compounds **1a**, **2a**, **3a** and **4a** (top to bottom). The red lines plot the voltammograms measured with a switching potential immediately past the first reduction or oxidation. Arrows indicate the direction of the scan.

Cyclic voltammetry for compounds **1a**, **2a**, **3a** and **4a** reveals between two and four resolved oxidation processes (labelled *ox1* to *ox4*) and two reduction processes (labelled *red1* and *red2*) in the accessible potential window. In each case the initial potential was selected to coincide with the measured rest potential and the position of zero current in the RDE voltammograms confirms the nature of the processes as oxidations or reductions. The mid-point potentials (E_m) tabulated in Table 3 were calculated by taking the average of the oxidation and reduction peak potentials (E_p) from the cyclic voltammograms. Where possible, the peak-to-peak separations (ΔE_p) are also tabulated, as are the half-wave potentials ($E_{1/2}$) and limiting current values (i_L) from RDE

voltammetry. The first oxidation (*ox1*) is a chemically reversible and diffusion controlled 1e-processes for **1a**, **2a** and **4a**; the ratio of oxidative and reductive currents for these processes are close to unity and the ΔE_p values at a scan rate of 100 mVs^{-1} are 80 mV or less. Process *ox1* is assigned as the 1e-oxidation of the $dbcat^{2-}$ ligand to $dbsq^{-}$ based on the analogous process in $[Fe^{III}(L\text{-}N_4Me_2)(dbdiox)]^{n+}$.[14] This process is irreversible and at a more positive potential for Mn compound **3a**, possibly suggesting instability of the Mn(III)-dbsq analogue. The cyclic voltammograms suggest the first reduction process *red1* is electrochemically reversible for all four compiounds and associated with 1e-reduction (ΔE_p values all less than 85 mV). This process is assigned as the metal-based reduction of trivalent metals ions to divalent ions in the $[M^{III}(L\text{-}N_4R_2)(dbcat)]^{2+}$ complexes.[14,16,19] In all cases, the limiting currents in the RDE voltammograms for *ox1* and *red1* are very similar (Table 3), consistent with both processes involving the transfer of one electron. A second irreversible (**1a**) or quasi-reversible (**3a**, **4a**) process, *red2*, is evident at much more negative potentials and is assigned as originating from the pyridinophane ligands, the RDE limiting currents suggest that this may also be a 1e-process.[19] For all compounds, the second oxidation, *ox2,* is irreversible and assigned to the oxidation of the tetraphenylborate counterion.[63] The remaining oxidations, *ox3* and *ox4*, show some degree of reversibility in terms of current response on the reverse sweep for compounds **1a** and **3a**. Processes *ox2* and *ox3* are merged in the RDE voltammograms. Definitive assignment of processes *ox3* and *ox4* is not possible, but it is likely that one of these processes is due to oxidation of the $dbsq^{-}$ ligand to the neutral benzoquinone form, while another process may be attributed to the 1e-oxidation from the trivalent to the tetravalent metal ion.

Table 3 Cyclic and RDE voltammetry data for acetonitrile (0.25 M Bu_4NPF_6) solutions of compounds **1a**, **2a**, **3a** and **4a**.[a]

	Cyclic voltammetry data E_m or E_p / V, (ΔE_p / mV)				RDE voltammetry data $E_{1/2}$ [a] / V, (i_L / μA)			
Redox process	**1a**	**2a**	**3a**	**4a**	**1a**	**2a**	**3a**	**4a**
ox1	-0.15 (70)	-0.14 (80)	0.22 [b]	0.01 (80)	-0.16 (28)	-0.14 (29)	0.17 (28)	0.01 (28)
ox2	0.46 [b]	0.47 [b]	0.46 [b]	0.45 [b]	0.42 (64)	0.40 (66)	0.44 (61)	0.43 (76)
ox3	0.85 (90)	0.92 [b]	0.61 [b]	.65 [b]	0.88 (28)	0.91 (28)	-	-
ox4	1.13 [b]	1.15 [b]	-	1.11 (95)	-	-	-	-
red1	-0.89 (65)	-1.00 (85)	-0.92 (65)	-1.02 (75)	-0.88 (35)	-1.01 (34)	-0.92 (36)	-1.02 (35)
red2	-2.50 [b]	-2.44 [b]	-2.45 (70)	-2.03 (80)	-2.47 (34)	-2.43 (33)	-2.45 (41)	-2.44 (39)
Δ(*ox1-red1*)	0.74	0.85	-	1.02	0.72	0.87	1.09	1.03

[a] All potentials are referenced *versus* the ferrocene/ferrocenium couple.

[b] E_p rather than E_m reported at 100 mV s^{-1} scan rates.

For metal-dioxolene complexes that exhibit VT transitions, the separation in redox potential between the catecholate oxidation and metal-based reduction correlates with the accessibility and transition temperature of a VT interconversion.[55] The differences between the E_m values for *ox1* and *red2* are tabulated in Table 3. We have previously suggested that a Δ*(ox1-red1)* value of less than ~ 0.74 V is a good indicator for an accessible VT transition.[28] For the present family, the smaller separation of 0.73-0.74 V for **1a** versus 0.85-0.86 V for **2a** suggests that complex **1** is more likely to exhibit a VT transition than **2**. It would be interesting to compare these values to the corresponding values for literature complexes **5** and **6**, however the reported voltammetry is incomplete as the metal-based processes were not reported.[13] A reversible process equivalent to *ox1* was observed for **5** at -0.11 V versus Fc/Fc^+, while the dbdiox-based process for **6** is instead a reversible 1e-reduction from $dbsq^-$ to $dbcat^{2-}$ at -0.80 V versus Fc/Fc^+. For the Co(III) complexes, the redox potential of this process thus decreases monotonically as the pyridinophane alkyl substituent is varied from methyl to ethyl to *iso*-propyl, while for the *tert*-butyl substituent, the relative potentials of the most accessible metal- and ligand-based processes swap and the preferred state of the complex is instead Co(II)-dbsq. Some of us reported a similar swapping of the cobalt and dioxolene based redox processes for the $[Co_2(spiro)(Me_ntpa)_2]^{2+}$ family (tpa = tris(2-pyridylmethyl)amine, Me_ntpa involves successive methylation of the 6-position of the pyridine rings).[24]

Solid State Magnetic Measurements

Magnetic susceptibility data were collected on crushed crystalline samples of **1a**·dioxane, **2a**·2dioxane, **3a**·1.5dioxane and **4a**·dioxane with an applied field of 0.1 T. For **1a**·dioxane and **2a**·2dioxane data were collected upon cooling from 200 K to 2 K, then heating from 2 K to 400 K and finally cooling from 400 K back down to 2 K; for **3a**·1.5dioxane and **4a**·dioxane data were collected upon cooling from 200 K to 2 K and then upon heating up to 340 K. The data

obtained upon first cooling and heating overlay within error in all cases. Magnetization data for **3a**·1.5dioxane and **4a**·dioxane were measured at 2 and 4 K with magnetic fields up to 5 T.

Compound **1a**·dioxane is diamagnetic between 2 K and 200 K, with a small $\chi_M T$ product value of 0.1-0.2 cm^3 K mol^{-1} (Fig. 5), which is consistent with a LS-Co(III)-dbcat formulation. As the temperature increases above 200 K there is sharp increase in the $\chi_M T$ product, indicating the formation of a paramagnetic species and consistent with the onset of a VT interconversion. At the highest measured temperature of 400 K the transition is incomplete and the $\chi_M T$ product is 0.55 cm^3 K mol^{-1}, much less than the value of 3.0-3.8 cm^3 K mol^{-1} expected for the HS-Co(II)-dbsq complex that would arise from a complete VT transition.[55,64–66] Upon cooling from 400 K back down to 2 K, the $\chi_M T$ profile is similar to the initial data set although the values are around 0.04 $cm^3 mol^{-1}$ K higher. The discrepancy in profiles on heating and cooling above room temperature is likely due to desolvation, but is still suggestive of reversibility of the VT interconversion. For compound **2a**·2dioxane, the $\chi_M T$ product value of 0 cm^3 K mol^{-1} at 2 K increases gradually to 0.15 cm^3 K mol^{-1} at 400 K. This is consistent with a diamagnetic LS-Co(III)-dbcat formulation across the entire temperature range with the presence of a temperature-independent-paramagnetism contribution, that is well-known for Co(III).[67] While VT interconversions in cobalt-dioxolene complexes can also be induced by irradiation with visible light at low temperatures,[10] equivalent photo-induced SCO has yet to be reported for cobalt complexes that exhibit thermally-induced SCO.[68] In the present case, the high temperature of the onset of the thermally-induced VT interconversion for **1a** renders photo-induced VT unlikely and photomagnetic studies were not pursued.[26,69]

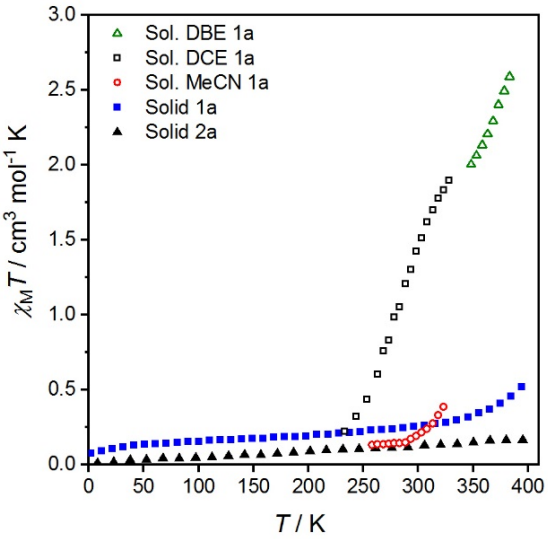

Fig. 5 Solid state (SQUID) $\chi_M T$ versus T plots for **1a**·dioxane (■) and **2a**·2dioxane (▲), and solution (Evans NMR) data for **1a**·dioxane in 1,2-dichloroethane-d_4 (□), 1,2-dibromoethane-d_4 (△) and acetonitrile-d_3 (○).

For **3a**·1.5dioxane the $\chi_M T$ product (Fig. 6) has a value of 3.0 cm^3 K mol^{-1} at 340 K and is temperature-independent as the temperature decreases, before decreasing below 25 K to a value of 2.0 cm^3 K mol^{-1} at 2 K. The high temperature $\chi_M T$ value is consistent with the HS-Mn(III)-dbcat (S = 2) formulation. Although the {N_4O_2} donor set affords SCO interconversions for Mn(III) in some cases,[70,71] there is no sign of any thermally-induced transition for **3a**. The rapid decrease in $\chi_M T$ below 25 K is consistent with zero-field-splitting (ZFS). The reduced magnetization (Fig. S5) plots at 2 and 4 K do not saturate and the isotherms are not superimposed, suggesting considerable anisotropy. The susceptibility and magnetization data were simultaneously fit to a zero-field splitting (ZFS) Hamiltonian using PHI,[37] for the Landé g-factor, axial ZFS parameter (D) and a rhombic ZFS term (E). Two comparable fits were obtained with g = 1.99(1), D = -3.63(7) cm^{-1} and E = -1.1(1) cm^{-1} or D = 3.77(1) cm^{-1} and E =1.0(1) cm^{-1}, suggesting significant rhombic anisotropy. Determining ZFS parameters from powder magnetic data is not a reliable method and a spectroscopic technique,

such as high field EPR spectroscopy, would be required to verify the magnitude and sign of the ZFS parameters,[72,73] which is beyond the scope of the present work. For comparison, high field EPR studies of the related pyridinophane HS-Mn(III) complex $[Mn(L\text{-}N_4iPr_2)F_2]^+$ afforded $S = 2$, $D = -3.79$ cm^{-1}, with slight rhombicity $|E/D| = 0.02–0.04$, in particular confirming the negative sign of D.[19] For complex **3**, the higher rhombicity may result from structural effects associated with the chelating dioxolane co-ligand and indeed according to our continuous shape measurements,[51] complex **3** in **3a**·1.5dioxane is more distorted from octahedral than $[Mn(L\text{-}N_4iPr_2)F_2]^+$.

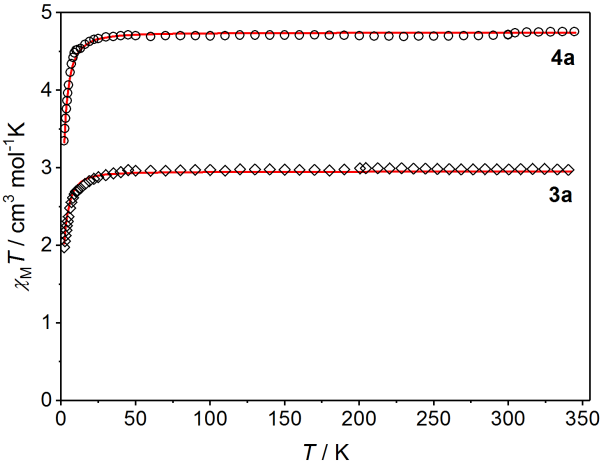

Fig. 6 Plots of $\chi_M T$ measured for **3a**·1.5dioxane (◊) and **4a**·dioxane (○) in the solid state, the lines are best fits as described in the text.

For **4a**·dioxane, the thermal-dependence of $\chi_M T$ is qualitatively similar to that observed for **3a**·1.5dioxane (Fig. 6). The $\chi_M T$ value of 4.7 cm^3 K mol^{-1} between 25 and 340 K is consistent with the HS-Fe(III)-dbcat (S = 5/2) ground state suggested by the 100 K structural data measured for **4a**·2MeOH. There is no sign of a SCO or VT transition, despite the fact that the $\{N_4O_2\}$ donor set sometimes affording SCO for Fe(III).[74–76] Below 25 K, $\chi_M T$ decreases to a value of 3.3 cm^3 K mol^{-1} at 2 K. As for **3a**, the 2 and 4 K isotherms in the reduced magnetization plots

for **4a** do not superimpose (Fig. S5), again suggesting considerable single ion anisotropy. Simultaneously fitting the susceptibility and magnetization data required only the inclusion of axial ZFS, affording $g = 2.07(1)$ and $D = 3.62(2)$ cm^{-1}, with this D value consistent with values reported previously for significantly distorted octahedral HS-Fe(III) complexes.[77,78] Efforts to fit the data with a negative D value afforded a poorer fit. Definitive determination of the sign of D might be possible with low temperature EPR spectroscopy.[79] The g value obtained from fitting the magnetic data is higher than the value of 2.0 expected for HS-Fe(III), which might be due to mixing of the HS-Fe(III)-dbcat with some HS-Fe(II)-dbsq component, as has been observed previously for iron catecholate systems.[80]

Solution State Magnetic Measurements

Solution magnetic susceptibility data were measured by the Evans NMR method on solutions of **1a**·dioxane in 1,2-dichloroethane-d_4, 1,2-dibromoethane-d_4 and acetonitrile-d_3 (Fig. 5). Data were measured across different temperatures ranges depending on the liquid range of the solvent and the solubility of the compound. In each case an increase in $\chi_M T$ is observed with increasing temperature, consistent with the onset of a VT interconversion in solution, however the transition is incomplete in all three solvents, with a largest measured $\chi_M T$ value of 2.6 cm^3 K mol^{-1}, compared to a value of around 3.2 cm^3 K mol^{-1} expected for a HS-Co(II)-dbsq species.[28] The transition temperature increases in the order 1,2-dichloroethane < 1,2-dibromoethane < acetonitrile. This solvent-dependence is consistent with the variable temperature solution electronic absorption spectra. Previous studies of both VT and SCO systems in solution have found that the transition temperature dependence does not simply follow the variation in dielectric constant, but instead can depend on specific solvent-complex interactions, including hydrogen bonding, that differ between the two electromers or spin states.[81–84] In the present case, the origin of the trend is not clear, but the lower transition temperature in chlorinated solvents

versus acetonitrile is consistent with observation for VT interconversions in other cobalt-dioxolene complexes.[28,82]

Mössbauer Spectroscopy

^{57}Fe Mössbauer spectra were measured for compound **4a**·dioxane as a function of temperature. The spectra show a single broad quadrupole doublet with parameters (δ = 0.43, ΔE_Q = 2.08 mm/s) consistent with HS-Fe(III) and therefore in agreement with the magnetic data. However, the asymmetry of the spectra is temperature dependent (Fig. 7) with the lower energy absorption broadened significantly at low temperatures (< 30 K) and the higher energy absorption broadened significantly at higher temperatures (> 30 K). Different samples and different sample preparation produced consistent and reproducible data. The origin of this effect is currently unknown, although it could be caused by an unusual Goldanskii-Karyagin effect and this will be investigated in future studies.[85] Similar asymmetry has been observed previously for iron(III)-catecholate complexes.[80,86]

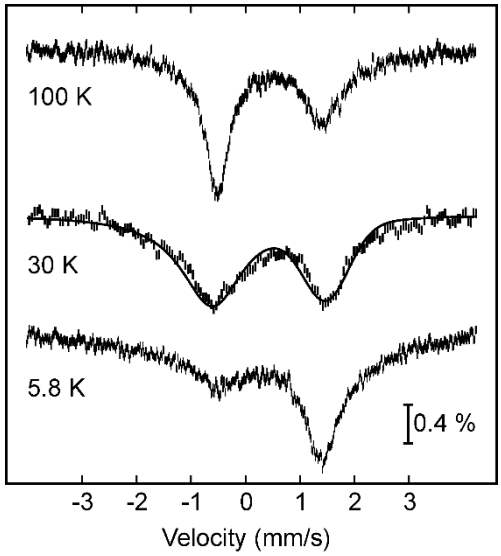

Fig. 7 Mössbauer spectra of **4a**·dioxane measured at various temperatures.

Related compounds investigated by Koch *et al*. show similar quadrupole splittings (ΔE_Q ~2.3 mm/s) but different isomer shifts, depending on whether the complex is LS-Fe(III) (δ = 0.18 mm/s)[14] or intermediate (S = 3/2) spin (IS)-Fe(III) (δ = 0.35 mm/s).[87] Compound **4a**·dioxane therefore follows the same trend of increasing isomer shift with increasing spin state. Further confirmation of our assignment was obtained by calculation of Mössbauer parameters for each of the spin states (Table S3) using the models obtained through DFT (see below). Comparison of the experimental Mössbauer parameters with the calculated ones also support a HS-Fe(III) center in **4a**·dioxane, consistent with magnetic data for this compound and the structural analysis of differently solvated **4a**·2MeOH.

Density Functional Theory Calculations

Density functional theory calculations have previously played an important role in elucidating VT transitions in dioxolene complexes.[28,45–47,88–90] Calculations were performed on compounds **1a**, **2a**, **3a** and **4a**, including the monocationic metal complexes and counteranions and compared with calculations on the related literature cobalt compounds [Co(L-N_4Me_2)(dbdiox)](BF_4) (**5b**) and [Co(L-$N_4{}^tBu_2$)(dbdiox)](B(*p*-$C_6H_4Cl)_4$) (**6a**) (Fig. 8, Tables S4 and S5).[47]

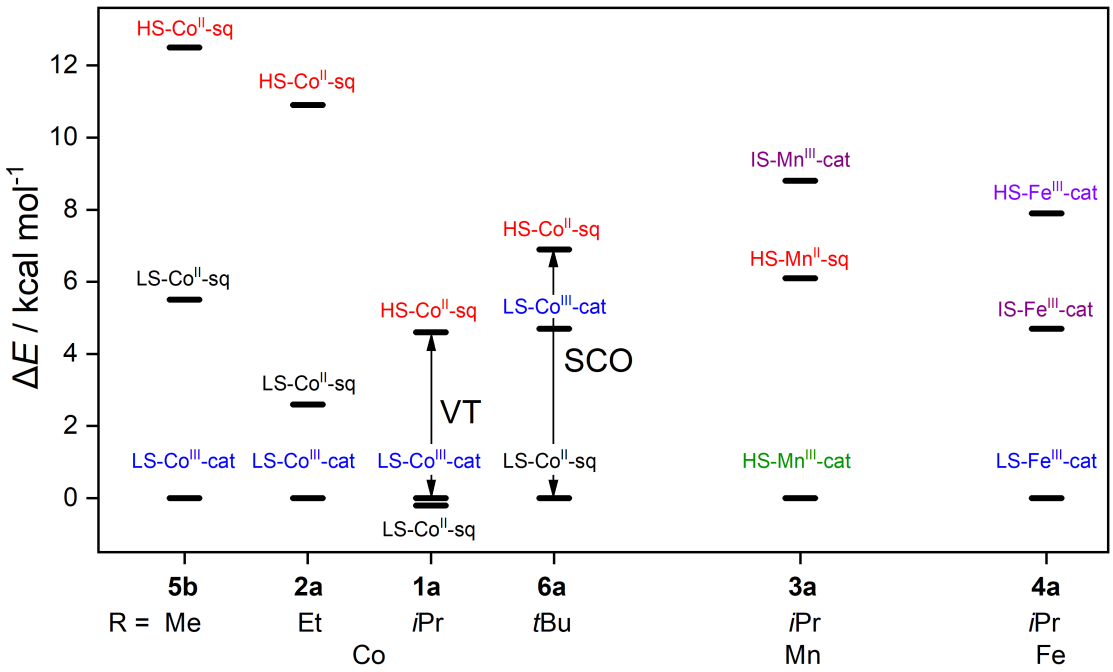

Fig. 8 Plots of relative energies calculated for compounds of the different electromeric forms of complexes **1**-**6**, $[M(L\text{-}N_4R_2)(dbdiox)]^+$, indicating observed VT and SCO interconversions for **1** and **6**, respectively.

Calculations of compound **1a** indicate the structure on the singlet potential energy surface (PES) corresponds to the ground state of this molecule. The absence of the bond alternation in the six-membered ring of the dbdiox ligand, the lengths of C–O bonds, equal to 1.36 Å, and the distances the between the cobalt center and ligand donor atoms (Fig. S7) are in excellent agreement with the 100 K X-ray data for **1a**·dioxane. The structural data point unambiguously to the LS-Co(III)-dbcat electronic isomer for complex **1**, which is also consistent with the magnetic data (Fig. 5). A LS-Co(II)-dbsq tautomer is also possible on the triplet PES and of comparable energy to LS-Co(III)-dbcat. However, the bond lengths calculated for the LS-Co(II)-dbsq electromer are not in good agreement with the experimentally measured values and the magnetic data are not consistent with the $S = 1$ ground state expected to arise from the strong ferromagnetic coupling between the LS-Co(II) ion and

the semiquinonate ligand, as found for the related complex [Co(L-N_4tBu_2)(dbdiox)]$^{+}$.[12] Thus, in comparison with experimental data we conclude that the ground state and low temperature form of complex **1** is the LS-Co(III)-dbcat electromer. The HS-Co(II)-dbsq electromer is destabilized with respect to the LS-Co(III)-dbcat ground state by 4.6 kcal mol^{-1}, which indicates the accessibility of this tautomer through a thermally-induced VT transition. The calculated bond lengths in this tautomer are not consistent with the values from 100 K X-ray data for **1a**·dioxane. The presence of two paramagnetic centers in the HS-Co(II)-dbsq form of the complex implies an exchange interaction. Calculations using the "broken symmetry" (BS) approach and Yamaguchi equation suggest antiferromagnetic exchange (J = -18 cm^{-1}) of moderate magnitude between unpaired electrons of the cobalt ion and the semiquinonate ligand.

Calculations of compound **2a** indicate that the ground state of complex **2** is the LS-Co(III)-dbcat electromer, the geometry characteristics of which are in a good agreement with the 130 K single crystal X-ray data (Fig. S8). The HS-Co(II)-dbsq electromer is destabilized compared to the LS-Co(III)-dbcat electromer by 10.9 (8.2 taking zero point energy (ZPE) into account) kcal mol^{-1}, which allows us to expect the possible onset of a VT interconversion around the highest experimentally accessible temperatures, consistent with variable temperature solution electronic absorption spectra and magnetic susceptibility measurements (Figs. 4 and 6). As per **1**, the HS-Co(II)-dbsq electromer is characterized by antiferromagnetic coupling of spins of unpaired electrons of the metal ion and the semiquinonate ligand.

It is informative to compare the computational results for the L-N_4iPr_2 complex **1** and L-N_4Et_2 complex **2** with the results previously reported by one of us for the related complexes **5** and **6**,[47] to assess the role of the alkyl substituents on the 2,11-diaza[3.3](2,6)pyridinophane ligands on the electronic lability of the cobalt complexes. For tetrafluoroborate salt **5b**, the

closed-shell LS-Co(III)-dbcat isomer on the singlet PES is the ground state,[47] consistent with experimental data measured for the tetraphenylborate compound **5a**·0.8MeCN·0.2Et_2O.[12] In contrast, calculations for **6a** indicate a LS-Co(II)-dbsq isomer in the ground state capable of a SCO transition to the HS-Co(II)-dbsq electromer,[47] which was observed experimentally.[12,46] Comparison of the energies of the three tautomers for the four cobalt complexes is interesting (Fig. 8). As the alkyl substituents on the pyridinophane ligand increases in bulk from methyl (**5**) to ethyl (**2**) to *iso*-propyl (**1**), the LS-Co(II)-dbsq and HS-Co(II)-dbsq both decrease in energy relative to the LS-Co(III)-dbcat, with a VT interconversion thus most favorable for **1**. Upon further increase to the *tert*-butyl substituents in **6**, there is a reversal in the energies, with the LS-Co(II)-dbsq electromer stabilized by 4.7 kcal mol^{-1} over the LS-Co(III)-dbcat form, establishing the conditions for SCO for **6** rather than the VT transition that is evident for **1**. According to the calculation results of the BS states, the variation of alkyl subsitituents on the pyridinophane ligands does not significantly impact the nature of the exchange interactions in the isomers of cobalt complexes **1**, **2**, **5** and **6**: the HS-Co(II)-dbsq electromer is characterized by moderate antiferromagnetic exchange in all cases compared to very strong ferromagnetic exchange for the LS-Co(II)-dbsq tautomers (Table S4).

For the manganese compound **3a**, three redox isomers were found by DFT. The minimum on the quintet PES corresponds to the most stable state. The spin density distribution and dioxolene bond lengths point to the HS-Mn(III)-dbcat electromer (Fig. S9), consistent with the magnetic susceptibility and magnetization data (Figs. 6 and S4). The structural characteristics calculated for this electromer are in good agreement with the X-ray data. Geometry optimization on the septet PES affords the HS-Mn(II)-dbsq electromer, with a calculated coupling constant of J = -225 cm^{-1}, indicating strong antiferromagnetic exchange interactions stabilizing the S = 2 state. The energy difference between the BS state of the HS-Mn(II)-dbsq structure and the HS-Mn(III)-dbcat electromer is 6.1 kcal mol^{-1}. Another

electromer of **3**, intermediate spin IS-Mn(III)-dbcat, is localized on the triplet PES and destabilized with respect to the ground electronic state by 8.8 kcal mol^{-1}, while all attempts to find a LS-Mn(III)-dbcat electromer resulted in structures with unstable DFT wave functions. Thus, a VT transition is possible in the manganese complex above room temperature, but it will not be accompanied by large changes of the magnetic characteristics in view of strong antiferromagnetic exchange in the isomer HS-Mn(II)-dbsq.[6,58,59,61] As expected, the variable temperature magnetic data are consistent with an $S = 2$ ground state from 2 to 340 K, with no discontinuities suggestive of a structural transition that would accompany a VT or SCO interconversion. The room temperature electronic absorption spectra are consistent with the HS-Mn(III)-dbcat electromer suggested by the 130 K crystal structure. Variable temperature electronic absorption spectra indicate no change in butyronitrile solution in the temperature range 283-333 K.

For the iron compound **4a**, according to DFT calculations the HS-Fe(III)-dbcat electromer is localized on the sextet PES (Fig. S10). As often happens with iron complexes of dioxolene ligands, the calculated bond lengths for the latter have intermediate values between the expected catecholate and semiquinonate oxidation states.[91,92] The value of spin density at the metal ion is also ambiguous. Instead of a value close to 5 for HS-Fe(III), it is equal to 3.82 (Table S5). The calculated spin density distribution is an intermediate value between the HS-Fe(III)-dbcat and HS-Fe(II)-dbsq states. All attempts to find pure HS-Fe(III)-dbcat and HS-Fe(II)-dbsq electromers resulted in structures with unstable DFT wave functions. Similar complicated situations have been reported following DFT studies of related $[(tpa)Fe(diox)]^{+}$ (tpa = tris(2-pyridylmethyl)amine and diox = unsubstituted catecholate or semiquinonate), with the high spin electronic structure found to consist of a mixture of Fe(III)–catecholate and Fe(II)–semiquinonate configurations.[80] In the present case, the lowest energy electromer was found to be the LS-Fe(III)-dbcat with the IS-Fe(III)-dbcat next highest in energy. However,

the experimental bond lengths determined at 100 K for **4a**·MeOH (Table 2) are in closest agreement with the values calculated (optimized geometry) for HS-Fe(III)-dbcat, which is also consistent with the magnetic susceptibility up to 340 K (Fig. 6), low temperature magnetization measurements (Fig. S5) and variable temperature Mössbauer spectroscopic data measured for **4a**·dioxane (Fig. 7).

For the assignment of the electrochemical processes, the geometry optimization of the cationic complexes in the reduced (*red*) and oxidized (*ox*) forms has been performed. In compounds **1a** and **2a**, removing an electron from the complex results in the formation of a LS-Co(III)-dbsq species, characterized by absence of spin density at the metal center and localization of one electron at the oxygen atoms of semiquinone fragment (Fig. S11). At the same time, adding an electron stabilizes a LS-Co(II)-dbcat form with almost equivalent C-C bonds on the dioxolene fragment and one unpaired electron at the metal center. In the case of manganese and iron compounds **3a** and **4a**, 1e-reduction of the complexes leads to the HS-M(II)-dbcat electromer, while 1e-oxidation affords the IS-M(III)-dbsq or HS-M(III)-dbsq states (Fig. S12). Thus, analysis of spin density distributions and the calculated bond lengths of the dioxolene fragments unambiguously indicate that for all four complexes, the first 1e-reduction is metal-centered, while the first 1e-oxidation occurs at the ligand. The calculated (Table S6) differences between the redox potential ($\Delta(ox1\text{-}red1)$) for couples $\mathbf{1}^{0}/\mathbf{1}^{+}$ ($\mathbf{2}^{0}/\mathbf{2}^{+}$) and $\mathbf{1}^{+}/\mathbf{1}^{2+}$ ($\mathbf{2}^{+}/\mathbf{2}^{2+}$) are equal to 0.76 V and 0.87 V for **1a** and **2a**,[93,94] respectively, which are in excellent agreement with the measured values of 0.73 and 0.86 V (Table 3).

Concluding Remarks

A convenient synthetic route has been developed to complexes $[M(L\text{-}N_4iPr_2)(dbdiox)]^{+}$ (M = Co, Mn and Fe) and $[Co(L\text{-}N_4Et_2)(dbdiox)]^{+}$. Single crystal X-ray diffraction data for all

complexes at liquid nitrogen temperatures suggest trivalent metal cations and dioxolene ligands in the catecholate state. Variable temperature magnetic susceptibility data are consistent with these redox states for all complexes between 2 and 340 K with low spin configurations for the cobalt(III) ions and high spin configuration for the manganese(III) and iron(III) ions. However, above 340 K, $[Co(L\text{-}N_4iPr_2)(dbdiox)]^+$ exhibits an increase in magnetic susceptibility, suggesting the onset of a VT interconversion to a HS-Co(II)-dbsq tautomer that is far from complete at the highest temperature measured of 400 K. In solution, variable temperature electronic absorption spectra in different solvents are temperature-invariant for the manganese and iron complexes, indicating neither SCO nor VT for these complexes. In contrast, changes consistent with reversible VT interconversions are clearly evident for $[Co(L\text{-}N_4iPr_2)(dbdiox)]^+$ in several solvents. The spectra for $[Co(L\text{-}N_4Et_2)(dbdiox)]^+$ in 1,2-dichloroethane also suggest the onset of a VT transition at the highest temperatures. Solution state magnetic susceptibility measurements of $[Co(L\text{-}N_4iPr_2)(dbdiox)]^+$ by the Evans NMR method confirm VT transitions, with solvent-dependent transition temperatures. The origin of the dependence of the VT transitions temperature on solvent is not clear, but lower transition temperatures are evident in halogenated solvents compared to organic nitriles.

Solution voltammetric measurements indicate rich redox chemistry for all four complexes. Notably the two cobalt complexes exhibit a reversible first oxidation that is ligand-based and first reduction that is metal-based. The potential separation between these processes is less for $[Co(L\text{-}N_4iPr_2)(dbdiox)]^+$ than for $[Co(L\text{-}N_4Et_2)(dbdiox)]^+$. The relative values for the two complexes are consistent with a proposition previously made by some of us, that VT transitions can be expected when the potential separation between the "frontier" ligand- and metal-based redox processes is less than around 740 mV.[28]

Density functional theory calculations have provided important insights in this work. For the cobalt and manganese complexes the relative energies calculated for the different electronic isomers, and the comparison of calculated structural parameters versus experimental values, have confirmed the redox and spin state of the complexes as LS-Co(III)-dbcat and HS-Mn(III)-dbcat. As has been reported previously for related complexes, the situation is less clear-cut in the iron case. However Mössbauer spectra and magnetic susceptibility data are consistent with temperature-invariant HS-Fe(III)-dbcat and the experimental structural parameters are closest to those calculated for this electromer.

For the cobalt complexes $[Co(L\text{-}N_4R_2)(dbdiox)]^+$, it is interesting to compare the new R = Et and ^{i}Pr analogues, with the R = Me and ^{t}Bu compounds reported previously. Both *iso*-propyl and *tert*-butyl complexes exhibit thermally-induced electronic interconversions, but these are different. The *tert*-butyl complex undergoes a SCO transition from LS-Co(II)-dbsq to HS-Co(II)-dbsq, while the *iso*-propyl species displays a VT transition from LS-Co(III)-dbcat to HS-Co(II)-dbsq. The methyl and ethyl analogues exist in essentially temperature-independent LS-Co(III)-dbcat forms, although signs of a possible VT transition are evident for the ethyl analogue at the highest accessible temperatures. These observations are entirely consistent with the changes in the relative energies of the three electromers calculated by DFT for the four complexes. On increasing the steric bulk of the pyridinophane substituents from methyl to ethyl to *iso*-propyl, both the LS-Co(II)-dbsq and HS-Co(II)-dbsq electromers monotonically decrease in energy relative to the lowest energy LS-Co(III)-cat electromer. On extending the series to *tert*-butyl, LS-Co(II)-dbsq definitively takes over from LS-Co(III)-cat as the lowest energy electromer, while the energy of the HS-Co(II)-dbsq electromer increases.

This work represents the first systematic study of a series of members of a structural family of cobalt-dioxolene complexes that can exhibit thermally-induced SCO or VT

transitions. By combining experimental investigations with DFT calculations, we have been able to elucidate how the relative energies of the different electomeric forms vary with the steric bulk of the substituents on the non-dioxolene co-ligand. Key to the unusual behavior for this family of cobalt-dioxolene complexes is the highly constrained nature of the 12-membered pyridinophane azamacrocyclic ligands, which can facilitate SCO as well as the more commonly observed VT interconversions.

Acknowledgements

CB thanks the Australian Research Council for financial support (DP150100353). ECS acknowledges financial support from the Spanish Government, (Grant CTQ2015-68370-P). AS thanks the Ministry of Science and Higher Education of the Russian Federation (State assignment no. 4.1774.2017/4.6). Part of this research was undertaken on the MX1 beamline at the Australian Synchrotron, Victoria, Australia. Thanks to Dr Roger Mulder for his assistance with collecting the variable temperature NMR data.

Notes and references

[a] *School of Chemistry, University of Melbourne, Melbourne, 3010, Victoria, Australia. E-mail: c.boskovic@unimelb.edu.au*

[b] *Departament de Química Inorgànica i Orgànica, Universitat de Barcelona, Diagonal 645, 08028 Barcelona, Spain and Institut de Nanociència i Nanotecnologia, IN2UB, Universitat de Barcelona, 08028, Barcelona, Spain*

[c] *Institute of Physical and Organic Chemistry, Southern Federal University, 194/2 Stachka Ave. 344090 Rostov on Don, Russian Federation*

† Electronic Supplementary Information (ESI) available: additional structural information; infrared, electronic and Mössbauer spectral information; magnetic data and DFT results. CCDC reference numbers 1906460-1906463. For ESI and crystallographic data in CIF or other electronic format see DOI: 10.1039/b000000x/

References

1 K. Senthil Kumar and M. Ruben, *Coord. Chem. Rev.*, 2017, **346**, 176–205.

2 O. Sato, *Nat. Chem.*, 2016, **8**, 644–656.

3 A. Calzolari, Y. Chen, G. F. Lewis, D. B. Dougherty, D. Shultz and M. B. Nardelli, *J. Phys. Chem. B*, 2012, **116**, 13141–8.

4 P. Gütlich and H. A. Goodwin, *Top. Curr. Chem.*, 2004, **234**, 156–198.

5 M. A. Halcrow, *Spin Crossover Materials: Properties and Applications*, John Wiley & Sons, 2013.

6 D. N. Hendrickson and C. G. Pierpont, *Top. Curr. Chem.*, 2004, **234**, 63–95.

7 E. Evangelio and D. Ruiz-Molina, *Eur. J. Inorg. Chem.*, 2005, 2957–2971.

8 T. Tezgerevska, K. G. Alley and C. Boskovic, *Coord. Chem. Rev.*, 2014, **268**, 23–40.

9 J.-F. Létard, *J. Mater. Chem.*, 2006, **16**, 2550–2559.

10 O. Sato, A. Cui, R. Matsuda, J. Tao and S. Hayami, *Acc. Chem. Res.*, 2007, **40**, 361–9.

11 H. J. Krüger, *Chem. Ber.*, 1995, **128**, 531–539.

12 M. Graf, G. Wolmershäuser, H. Kelm, S. Demeschko, F. Meyer and H.-J. Krüger, *Angew. Chem. Int. Ed. Engl.*, 2010, **49**, 950–3.

13 F. Rupp, K. Chevalier, M. Graf, M. Schmitz, H. Kelm, A. Grün, M. Zimmer, M. Gerhards, C. van Wüllen, H.-J. Krüger and R. Diller, *Chem. Eur. J.*, 2017, **23**, 2119–2132.

14 W. O. Koch, V. Schünemann, M. Gerdan, A. X. Trautwein and H.-J. Krüger, *Chem.*

Eur. J., 1998, **4**, 1254–1265.

15 H.-J. Krüger, *Coord. Chem. Rev.*, 2009, **253**, 2450–2459.

16 B. Albela, R. Carina, C. Policar, S. Poussereau, J. Cano, J. Guilhem, L. Tchertanov, G. Blondin, M. Delroisse and J. J. Girerd, *Inorg. Chem.*, 2005, **44**, 6959–6966.

17 W. T. Lee, S. Xu, D. A. Dickie and J. M. Smith, *Eur. J. Inorg. Chem.*, 2013, 3867–3873.

18 W. T. Lee, S. B. Muñoz, D. A. Dickie and J. M. Smith, *Angew. Chemie Int. Ed.*, 2014, **53**, 9856–9859.

19 S. Xu, L. Bucinsky, M. Breza, J. Krzystek, C.-H. Chen, M. Pink, J. Telser and J. M. Smith, *Inorg. Chem.*, 2017, **56**, 14315–14325.

20 J. R. Khusnutdinova, N. P. Rath and L. M. Mirica, *Inorg. Chem.*, 2014, **53**, 13112–29.

21 A. Madadi, M. Itazaki, R. W. Gable, B. Moubaraki, K. S. Murray and C. Boskovic, *Eur. J. Inorg. Chem.*, 2015, 4991–4995.

22 Y. Mulyana, G. Poneti, B. Moubaraki, K. S. Murray, B. F. Abrahams, L. Sorace and C. Boskovic, *Dalton Trans.*, 2010, **39**, 4757–4767.

23 K. G. Alley, G. Poneti, J. B. Aitken, R. K. Hocking, B. Moubaraki, K. S. Murray, B. F. Abrahams, H. H. Harris, L. Sorace and C. Boskovic, *Inorg. Chem.*, 2012, **51**, 3944–3946.

24 K. G. Alley, G. Poneti, P. S. D. Robinson, A. Nafady, B. Moubaraki, J. B. Aitken, S. C. Drew, C. Ritchie, B. F. Abrahams, R. K. Hocking, K. S. Murray, A. M. Bond, H. H. Harris, L. Sorace and C. Boskovic, *J. Am. Chem. Soc.*, 2013, **135**, 8304–8323.

25 O. Drath, R. W. Gable, B. Moubaraki, K. S. Murray, G. Poneti, L. Sorace and C. Boskovic, *Inorg. Chem.*, 2016, **55**, 4141–4151.

26 O. Drath, R. W. Gable, G. Poneti, L. Sorace and C. Boskovic, *Cryst. Growth Des.*, 2017, **17**, 3156–3162.

27 O. Drath, R. W. Gable and C. Boskovic, *Acta Cryst. Sect.*, 2018, **C74**, 734–741.

28 G. K. Gransbury, M. E. Boulon, S. Petrie, R. W. Gable, R. J. Mulder, L. Sorace, R. Stranger and C. Boskovic, *Inorg. Chem.*, 2019, **58**, 4230–4243.

29 I. M. Piglosiewicz, R. Beckhaus, G. Wittstock, W. Saak and D. Haase, *Inorg. Chem.*, 2007, **46**, 7610–7620.

30 C.-M. Che, Z.-Y. Li, K.-Y. Wong, C.-K. Poon, T. C.W.Mak and S.-M. Peng, *Polyhedron*, 1994, **13**, 771–776.

31 A. J. Wessel, J. W. Schultz, F. Tang, H. Duan and L. M. Mirica, *Org. Biomol. Chem.*, 2017, **15**, 9923–9931.

32 Crysalis Pro, Rigaku Oxford Diffraction. 2015.

33 N. P. Cowieson, D. Aragao, M. Clift, D. J. Ericsson, C. Gee, S. J. Harrop, N. Mudie, S. Panjikar, J. R. Price, A. Riboldi-Tunnicliffe, R. Williamson and T. Caradoc-Davies, *J. Synchrotron Radiat.*, 2015, **22**, 187–190.

34 O. V. Dolomanov, L. J. Bourhis, R. J. Gildea, J. A. K. Howard and H. Puschmann, *J. Appl. Cryst*, 2009, **42**, 339–341.

35 G. M. Sheldrick, *Acta Cryst.*, 2015, **71**, 3–8.

36 G. M. Sheldrick, *Acta Cryst.*, 2015, **71**, 3–8.

37 N. F. Chilton, R. P. Anderson, L. D. Turner, A. Soncini and K. S. Murray, *J. Comput. Chem.*, 2013, **34**, 1164–1175.

38 N. R. Council., *International Critical Tables of Numerical Data, Physics, Chemistry and Technology. Washington, DC: The National Academies Press.*, 1930.

39 S. Ranjbar, K. Fakhri and J. B. Ghasemi, *J. Chem. Eng. Data*, 2009, **54**, 3284–3290.

40 M. Geppert-Rybczyńska, A. Heintz, J. K. Lehmann and A. Golus, *J. Chem. Eng. Data*, 2010, **55**, 4114–4120.

41 M. Chorążewski, E. B. Postnikov, K. Oster and I. Polishuk, *Ind. Eng. Chem. Res.*, 2015, **54**, 9645–9656.

42 D. J. Frisch, M. J.; Trucks, G.W.; Schlegel, H. B.; Scuseria, G. E.; Robb, M. A.; Cheeseman, J. R.; Scalmani, G.; Barone, V.; Mennucci, B.; Petersson, G. A.; Nakatsuji, H.; Caricato, M.; Li, X.; Hratchian, H. P.; Izmaylov, A. F.; Bloino, J.; Zheng, G.; Sonnenbe, D. J. Gaussian 09. 2013.

43 G. E. C. the density functional ladder: N. meta-generalized gradient approximation designed for molecules and solids. Tao, J. M.; Perdew, J. P.; Staroverov, V. N.; Scuseria, *Phys. Rev. Lett.*, 2003, **91**, 146401.

44 J. P. Staroverov, V. N.; Scuseria, G. E.; Tao, J.; Perdew, *J .Chem. Phys.*, 2003, **119**, 12129–12137.

45 F. Bannwarth, A.; Schmidt, S. O.; Peters, G.; Sonnichsen, F. D.; Thimm, W.; Herges, R.; Tuczek, *Eur. J. Inorg. Chem.*, 2012, 2776–2783.

46 A. G. Starikov, A. A. Starikova and V. I. Minkin, *Dokl. Chem.*, 2016, **467**, 83–87.

47 A. A. Starikova, M. G. Chegerev, A. G. Starikov and V. I. Minkin, *Comput. Theor. Chem.*, 2018, **1124**, 15–22.

48 L. Noodleman, *J. Chem. Phys.*, 1981, **74**, 5737–5743.

49 K. Kitagawa, Y.; Saito, T.; Nakanishi, Y.; Kataoka, Y.; Matsui, T.; Kawakami, T.; Okumura, M.; Yamaguchi, *J. Chem. Phys.*, 2009, **113**, 15041.

50 G. A. Andrienko, Chemcraft - Graphical Software for Visualization of Quantum Chemistry Computations.

51 S. Alvarez, D. Avnir, M. Llunell and M. Pinsky, *New J. Chem.*, 2002, **26**, 996–1009.

52 W. O. Koch and H.-J. Krüger, *Angew. Chemie Int. Ed. Engl.*, 1995, **34**, 2671–2674.

53 S. N. Brown, *Inorg. Chem.*, 2012, **51**, 1251–1260.

54 P. T. Touceda, T. T. Patricia, S. M. Vázquez, M. V. Sandra, M. Lima, L. Manuela, A. Lapini, L. Andrea, P. Foggi, F. Paolo, A. Dei, D. Andrea, R. Righini and R. Roberto, *Phys. Chem. Chem. Phys.*, 2012, **14**, 1038–47.

55 A. Beni, A. Dei, S. Laschi, M. Rizzitano and L. Sorace, *Chem. Eur. J.*, 2008, **14**, 1804–13.

56 A. Caneschi, A. Dei, D. Gatteschi and V. Tangoulis, *Inorg. Chem.*, 2002, **41**, 3508–3512.

57 J. R. Khusnutdinova, J. Luo, N. P. Rath and L. M. Mirica, *Inorg. Chem.*, 2013, **52**, 3920–3932.

58 N. Shaikh, S. Goswami, A. Panja, X. Y. Wang, S. Gao, R. J. Butcher and P. Banerjee, *Inorg. Chem*, 2004, **43**, 5908–5918.

59 N. Shaikh, S. Goswami, A. Panja, H. H. H. Sun, F. Pan, S. Gao and P. Banerjee, *Inorg. Chem.*, 2005, **44**, 9714–9722.

60 S. Goswami, A. Panja, R. J. Butcher, N. Shaikh and P. Banerjee, *Inorg. Chim. Acta*, 2011, **370**, 311–321.

61 A. Panja, *Inorg. Chem. Commun.*, 2012, **24**, 140–143.

62 P. Mialane, L. Tchertanov, F. Banse, J. Sainton and J. J. Girerd, *Inorg. Chem.*, 2000, **39**, 2440–2444.

63 P. K. Pal, S. Chowdhury, M. G. B. Drew and D. Datta, *New J. Chem.*, 2002, **26**, 367–371.

64 D. Ruiz-Molina, L. N. Zakharov, A. L. Rheingold and D. N. Hendrickson, *J. Phys. Chem. Solids*, 2004, **65**, 831–837.

65 A. Bencini, A. Beni, F. Costantino, A. Dei, D. Gatteschi and L. Sorace, *Dalton Trans.*, 2006, 722–9.

66 P. Dapporto, A. Dei, G. Poneti and L. Sorace, *Chem. Eur. J.*, 2008, **14**, 10915–8.

67 R. L. Carlin, *Magnetochemistry*, Springer-Verlag, 1986.

68 I. Krivokapic, M. Zerara, M. Daku, a Vargas, C. Enachescu, C. Ambrus, P. Tregennapiggott, N. Amstutz, E. Krausz and a Hauser, *Coord. Chem. Rev.*, 2007, **251**,

364–378.

69 A. Hauser, *Top. Curr. Chem.*, 2004, **234**, 155–198.

70 G. G. Morgan, K. D. Murnaghan, H. Müller-Bunz, V. McKee and C. J. Harding, *Angew. Chemie Int. Ed.*, 2006, **45**, 7192–7195.

71 S. Wang, Y.-J. Li, F.-F. Ju, W.-T. Xu, K. Kagesawa, Y.-H. Li, M. Yamashita and W. Huang, *Dalton Trans.*, 2017, **46**, 11063–11077.

72 S. Mossin, H. Weihe and A. L. Barra, *J. Am. Chem. Soc.*, 2002, **124**, 8764–8765.

73 J. Krzystek, A. Ozarowski and J. Telser, *Coord. Chem. Rev.*, 2006, **250**, 2308–2324.

74 F. Yu, Y. Zhang, A. Li and B. Li, *Inorg. Chem. Commun.*, 2015, **51**, 87–89.

75 D. J. Harding, P. Harding and W. Phonsri, *Coord. Chem. Rev.*, 2016, **313**, 38–61.

76 W. Phonsri, P. Harding, L. Liu, S. G. Telfer, K. S. Murray, B. Moubaraki, T. M. Ross, G. N. L. Jameson and D. J. Harding, *Chem. Sci.*, 2017, **8**, 3949–3959.

77 M. Go, I. Ferna, Ä. Gutie and J. J. Lucena, *Inorg. Chem.* 2006, **45**, 5321–5327.

78 S. Jana, A. Bhattacharyya, B. Nath, K. Rissanen, S. Herrero, R. Jiménez-Aparicio and S. Chattopadhyay, *Inorg.Chim. Acta*, 2016, **453**, 715–723.

79 J. J. Girerd, M. L. Boillot, G. Blain and E. Rivière, *Inorg. Chim. Acta*, 2008, **361**, 4012–4016.

80 A. J. Simaan, M. L. Boillot, R. Carrasco, J. Cano, J. J. Girerd, T. A. Mattioli, J. Ensling, H. Spiering and P. Gütlich, *Chem. Eur. J.*, 2005, **11**, 1779–1793.

81 W. Linert, M. Enamullah, V. Gutmann and R. F. Jameson, *Monatshefte für Chemie - Chem. Mon.*, 1994, **125**, 661–670.

82 E. Evangelio, C. Rodriguez-Blanco, Y. Coppel, D. N. Hendrickson, J. P. Sutter, J. Campo and D. Ruiz-Molina, *Solid State Sci.*, 2009, **11**, 793–800.

83 S. A. Barrett, C. A. Kilner and M. A. Halcrow, *Dalton Trans.*, 2011, **40**, 12021–12024.

84 J. N. McPherson, R. W. Hogue, F. S. Akogun, L. Bondì, E. T. Luis, J. R. Price, A. L.

Garden, S. Brooker and S. B. Colbran, *Inorg. Chem.*, 2019, **58**, 2218–2228.

85 A. X. Gütlich, Philipp, Bill, Eckhard and Trautwein, *Mössbauer Spectroscopy and Transition Metal Chemistry*, Springer-Verlag Berlin Heidelberg, 2011.

86 S. Floquet, A. J. Simaan, E. Rivière, M. Nierlich, P. Thuéry, J. Ensling, P. Gütlich, J.-J. Girerd and M.-L. Boillot, *Dalton Trans.*, 2005, 1734–42.

87 A. X. Trautwein, W. O. Koch, H.-J. Krüger, M. Gerdan and V. Schünemann, *Chem. - A Eur. J.*, 2002, **4**, 686–691.

88 D. M. Adams, L. Noodleman and D. N. Hendrickson, *Inorg. Chem.*, 1997, **36**, 3966–3984.

89 D. Sato, Y. Shiota, G. Juhász and K. Yoshizawa, *J. Phys. Chem. A*, 2010, **114**, 12928–12935.

90 V. I. Minkin, A. Starikova and R. M. Minyaev, *Dalton Trans.*, 2013, **42**, 1726–34.

91 A. G. Minkin, V. I.; Starikov, *Russ. Chem. Bull.*, 2015, **64**, 475–497.

92 A. A. Minkin, V. I.; Starikov, A. G.; Starikova, *Pure Appl. Chem.*, 2018, **90**, 811–824.

93 L. E. Roy, E. Jakubikova, M. Graham Guthrie and E. R. Batista, *J. Phys. Chem. A*, 2009, **113**, 6745–6750.

94 A. V. Marenich, J. Ho, M. L. Coote, C. J. Cramer and D. G. Truhlar, *Phys. Chem. Chem. Phys.*, 2014, **16**, 15068–15106.

TOC Entry

Variation of alkyl substituents on pyridinophane ancillary ligands governs temperature-dependent valence tautomeric or spin crossover equilibria in a family of cobalt-dioxolene complexes.